Catalysis
Science & Technology

RSC Publishing

PAPER

View Article Online
View Journal | View Issue

Cite this: *Catal. Sci. Technol.*, 2013, **3**, 1333

Oxidative dehydrogenation of propane with nitrous oxide over Fe–MFI prepared by ion-exchange: effect of acid post-treatments†

Guangjun Wu, Fei Hei, Naijia Guan and Landong Li*

Received 14th November 2012,
Accepted 21st January 2013

DOI: 10.1039/c3cy20782j

www.rsc.org/catalysis

Fe–MFI prepared by reductive solution ion-exchange was investigated as catalyst for the oxidative dehydrogenation of propane with nitrous oxide, and a maximal propylene yield of *ca.* 14% could be obtained at the reaction temperature of 673 K. Accumulative acid post-treatments were performed on Fe–MFI and a gradual increase of maximal propylene yield to *ca.* 25% could be observed. The Fe–MFI samples before and after acid post-treatments were characterized by means of ICP, XRD, DRIFT, TEM, UV-Vis, H_2-TPR, NH_3-TPD and EPR. The results clearly indicated the transformation of iron species during acid post-treatments. The active iron species in Fe–MFI before and after acid post-treatments were characterized by FTIR spectra of NO adsorption. Based on the characterization and catalytic results, the extra-framework Fe–O–Al species and/or isolated iron species in Fe–MFI were proposed to be more active than oligonuclear iron species for propane dehydrogenation with nitrous oxide.

1. Introduction

Light olefins are very important components for the petrochemical industry and the market demand for light olefins has been growing steadily in recent years. The oxidative dehydrogenation of light paraffins provides a promising route to produce light olefins. In the past decades, the oxidative dehydrogenation of light paraffins to olefins, especially propane to propylene, has been extensively studied. Supported transition metal oxides, *e.g.* molybdenum oxides[1] and vanadium oxides,[2] are representative catalysts for the oxidative dehydrogenation of propane with dioxygen, and propylene yield of up to 30% can be obtained. For the oxidative dehydrogenation of propane with dioxygen, extensive CO_x is formed as over-oxidation by-product even at moderate propane conversion, and therefore low propylene selectivity and propylene yield are usually observed.

Nitrous oxide is an alternative promising oxidant especially when iron modified zeolites, *i.e.* iron–zeolites, are employed as catalysts. In general, nitrous oxide easily chemisorbs on the iron sites in zeolites, accompanied by the liberation of dinitrogen and the deposition of oxygen species.[3] The deposited oxygen species is highly active and can be used in several oxidation processes, *e.g.* benzene hydroxylation to phenol[4–7] and partial oxidation of methane to oxygenate.[8–10] In particular, it has been reported that the oxidative dehydrogenation of propane (ODHP) with nitrous oxide can be realized on iron–zeolite catalysts.[11–14] Several researches have been performed on the ODHP with nitrous oxide catalyzed by iron–zeolites, and the best results obtained are comparable with the ODHP with dioxygen catalyzed by transition metal oxides.[11–19] The use of nitrous oxide instead of dioxygen as oxidant in ODHP reaction distinctly decreases the required operation temperatures and improves the selectivity toward propylene. Moreover, nitrous oxide is a kind of harmful gas with strong greenhouse effect, and therefore the utilization of nitrous oxide from industrial emissions as raw reactant does make sense from an environmental point of view.

For the ODHP to propylene with nitrous oxide catalyzed by iron–zeolites, it is most important to know the active sites and the structure-activity relationship. The established knowledge on the active iron sites in ODHP reaction makes it possible to rationally design of highly active iron–zeolite catalysts. However, iron–zeolites are known to be complicated systems and many factors, *e.g.* the zeolite hosts employed and the preparation procedure, may strongly influence the nature and distribution of iron sites. The identification of specific iron sites in iron–zeolites and their role in the oxidative dehydrogenation of propane is therefore challenging. Notably, there are some puzzling disagreements on the active iron sites for the

Key Laboratory of Advanced Energy Materials Chemistry (Ministry of Education), College of Chemistry, Nankai University, Tianjin 300071, P. R. China.
E-mail: lild@nankai.edu.cn; Fax: (+)86 22 23500341; Tel: (+)86 22 23500341

† Electronic supplementary information (ESI) available. See DOI: 10.1039/c3cy20782j

ODHP with nitrous oxide. Bulánek *et al.*[12] claimed that the catalytic activity of Fe–ZSM-5 in the ODHP with nitrous oxide could be ascribed to the presence of extra-framework Fe–oxo complexes, similar to that reported by Panov *et al.*[3] in benzene hydroxylation with nitrous oxide. While Kondratenko *et al.*[14] proposed that oligonuclear iron species in Fe–ZSM-5 was more active than isolated iron species for the ODHP with nitrous oxide, probably due to the higher mobility of atomic oxygen species attached to oligonuclear iron species formed upon nitrous oxide chemisorption. Pérez-Ramírez *et al.*[15] suggested that traces of well-isolated iron species in Fe–ZSM-5 was extremely active in the ODHP with nitrous oxide, while large iron clusters enhanced the deep oxidation of important reaction intermediates to CO_x. Based on the literature reports, MFI is the most suitable zeolite host for iron species, and isomorphous substitution followed by high temperature steam-activation is the recommended route to prepare highly active Fe–MFI catalyst.[12–16] While other preparation routes, *e.g.* solution ion exchange and chemical vapor deposition, probably lead to low activity and selectivity.[15] In the present study, solution ion-exchange is employed as a simple and feasible means to prepare iron–zeolite for the ODHP with nitrous oxide. Accumulative acid post-treatments are performed on the as-prepared Fe–MFI to enhance the catalytic activity. The transformation of iron species in Fe–MFI during acid treatments is carefully characterized and the hints on the structure-activity relationship in the ODHP with nitrous oxide will be focused on.

2. Experimental section

2.1 Catalyst preparation

A series of alumino–silicate zeolites in H-Form with different framework structure were provided by Sinopec and employed as hosts for iron species. Prior to be used as hosts, the zeolite samples were heated to 873 K at a rate of 5 K min^{-1} and then calcined at 873 K in flowing air for 6 h. Fe–zeolite samples were prepared *via* liquid-phase ion exchange with ferrous salt. In a typical experiment, zeolite sample of 1 g was placed in the three-necked flask and exchanged with 100 mL of 0.1 M $FeCl_2$ aqueous solution for 24 h at room temperature under the protection of flowing nitrogen at 50 mL min^{-1}. The resulting solid was thoroughly washed with deionized water, dried at 353 K overnight, heated to 873 K at 5 K min^{-1} and calcined in flowing air at 873 K for 6 h. Fe–MFI sample was further subjected to acid post-treatment. For each acid treatment, sample of 1 g was treated with 100 mL of 0.01 M HCl solution at room temperature for 2 h. The resulting solid was thoroughly washed with deionized water, dried at 353 K overnight, heated to 873 K at 5 K min^{-1} and calcined in flowing air at 873 K for 6 h. The product was denoted as Fe–MFI-t*n*, where *n* indicated the accumulative times for the acid treatment.

2.2 Catalyst characterization

The Si, Al and Fe contents in samples were analyzed by a Perkin Elmer Optima 2000 inductively coupled plasma optical emission spectrometer (ICP-OES). The specific surface areas of samples were determined through low temperature N_2 adsorption–desorption isotherms collected on a Quantachrome iQ-MP gas absorption analyzer. The X-ray diffraction (XRD) patterns of samples were recorded on a Bruker D8 ADVANCE powder diffractometer using Cu-Kα radiation (λ = 0.1542 nm) at a scanning rate of 4° min^{-1} in the region of 2θ = 5–40°. Transmission electron microscopy (TEM) images were taken on a Philips Tecnai G2 20 S-TWIN electron microscope at an acceleration voltage of 200 kV. A few drops of alcohol suspension containing the sample were placed on a carbon-coated copper grid, followed by evaporation at ambient temperature. Diffuse reflectance infrared Fourier transform (DRIFT) spectra of samples were measured on a Bruker Tensor 27 spectrometer with 128 scans at a resolution of 2 cm^{-1}. A self-supporting pellet made of sample was placed in the reaction chamber (Praying Mantis CHC-CHA-3) and pretreated in flowing dry air at 473 K for 1 h. The spectra were recorded in dry air against KBr as background. The ^{27}Al solid-state magic angle spinning nuclear magnetic resonance (MAS-NMR) experiments were performed on a Bruker Avance III spectrometer at resonance frequencies of 104.3 MHz and with a sample spinning rate of 8 kHz. Diffuse reflectance ultraviolet-visible (UV-Vis) spectra of samples were recorded in the air against $BaSO_4$ in the region of 200–800 nm on a Varian Cary 300 UV-Vis spectrophotometer. To reduce light absorption, samples were diluted with $BaSO_4$ at a ratio of 1/4. The temperature-programmed desorption (TPD) experiments were carried out on a Quantachrome ChemBET 3000 chemisorption analyzer. Sample of *ca.* 0.1 g was pretreated in flowing He at 873 K for 1 h, cooled to 373 K in He and saturated with 5% NH_3/He. After that, the sample was purged with He for 30 min to eliminate the physisorbed ammonia. NH_3-TPD was then carried out in flowing He in the temperature range of 373–873 K at a heating rate of 10 K min^{-1}. The temperature-programmed reduction (TPR) experiments were carried out on a Quantachrome ChemBET 3000 chemisorption analyzer. Sample of *ca.* 0.1 g was pretreated in flowing oxygen at 873 K for 1 h, cooled to 323 K under same atmosphere and purged with 5% H_2/Ar for 30 min. H_2-TPR was then carried out in flowing 5% H_2/Ar in the temperature range of 323–923 K at a heating rate of 10 K min^{-1}. The response of the TCD to H_2 was calibrated by performing a TPR of CuO standard sample. Electron paramagnetic resonance (EPR) spectra in the X-band region were recorded with a Bruker EMX-6/1 spectrometer at 120 K with a microwave power of 5.0 mW and a modulation frequency of 100 kHz. 2,2-diphenyl-1-picrylhydrazyl hydrate (DPPH) was used as an internal standard for the measurement of the magnetic field. FTIR spectra with NO as probe were collected on a Bruker Tensor 27 spectrometer with 128 scans at a resolution of 2 cm^{-1}. A self-supporting pellet made of the catalyst sample was placed in the reaction chamber (Praying Mantis CHC-CHA-3) and pretreated in flowing He at 773 K for 1 h. After cooling to room temperature in flowing He, the He stream was switched to 1% NO/He and a series of time-dependent FTIR spectra were sequentially recorded.

2.3 Catalytic evaluation

The catalytic evaluation was performed in a fixed-bed flow micro-reactor at atmospheric pressure. Typically, 200 mg catalyst sample (sieve fraction of 0.17–0.25 mm) was placed in a quartz reactor (4 mm i.d.) and pretreated in 15% N_2O/He at

823 K for 1 h. After cooling to designed temperature, the reactant gas mixture (7.5% C_3H_8, 15% N_2O, and balance He) was fed to the reactor at a total flow rate of 50 mL min^{-1}, corresponding to a gas hourly space velocity (GHSV) of 15 000 h^{-1}. The steady-state tests were conducted isothermally at designed temperature and the gas products were analyzed after 15-min reaction by using two on-line gas chromatographs. One of them was equipped with a Plot Q capillary column and a FID detector for the analysis of organic products, the other with two packed columns (Porapak Q and Carbon Molecular Sieve TDX) and a TCD detector for the analysis of N_2O, N_2, O_2 and CO_x.

3. Results

3.1 Physico-chemical properties of Fe–zeolites

The ion exchange result and the physicochemical properties of Fe–MFI are summarized in Table 1. Theoretically, full ion exchange of zeolite by ferrous salt should give a Fe/Al ratio of 0.5. In the present work, extra-framework iron species can be introduced to the MFI host with Fe/Al ratios of 0.22 through primary solution ion exchange with ferrous salt. Further acid post-treatments on Fe–MFI result in the increase in Si/Al ratios and slight decrease in Fe loadings. These should be explained by the dealumination and leaching during acid post-treatments. Nevertheless, the Fe/Al ratios are kept at the similar level for Fe–MFI and acid treated Fe–MFI. It should be mentioned that chlorine is completely removed by thorough washing and subsequent calcination, and therefore no residual chlorine can be detected for all samples.

The powder XRD patterns of Fe–MFI samples employed in this study are shown in Fig. 1. Typical diffraction lines corresponding to MFI host are observed in Fe–MFI sample,[20] indicating that the framework structure of MFI host is well preserved after ion exchange and subsequent calcination. Besides, no obvious diffraction lines corresponding to iron species can be observed, probably due to the low Fe loadings. It is also clearly seen that the framework of MFI is well preserved for Fe–MFI even after accumulative acid post-treatments.

Fig. 2 displays the hydroxyl stretching region of DRIFT spectra of H–MFI and Fe–MFI samples. For H–MFI, a strong band at 3605 cm^{-1} corresponding to Brønsted acid hydroxyl groups, together with a weak band at 3740 cm^{-1} corresponding to silanol groups and a weak band at 3700 cm^{-1} corresponding to hydroxyl groups bounded to Lewis acid sites, can be observed.[21,22] With the introduction of iron species by ion exchange, the intensity of IR band corresponding to Brønsted acid hydroxyl groups decreases distinctly, while the intensities of IR bands corresponding to other hydroxyl groups are kept nearly unchanged. It is indicated that a large proportion of protons in Brønsted acid hydroxyl groups are replaced by cationic iron species. Acid post-treatments on Fe–MFI lead to the appearance of a new IR band at 3655 cm^{-1} corresponding to hydroxyl groups on extra-framework aluminum species[23] and the intensity of this IR band gradually increases with accumulative acid post-treatments. Obviously, acid post-treatments on Fe–MFI result in dealumination in the MFI framework.

The acidic properties of H–MFI and Fe–MFI are evaluated by NH_3-TPD and the results are shown in Fig. 3. For H–MFI, two major types of ammonia desorption peaks can be observed: the low-temperature peak centered at around 500 K corresponding to weak acid sites and high-temperature peak centered at around 700 K corresponding to strong acid sites. The high-temperature peak can be attributed to the desorption of NH_3 strongly interacting with the Brønsted acid sites in the specific case of Fe–MFI based on literature reports.[24–26] The introduction of iron species to H–MFI by ion exchange results in a distinct decrease in the amount of Brønsted acid sites due to the

Table 1 Physicochemical properties of Fe–MFI samples under study

Fe–zeolite	Zeolite host	Si/Al[a]	Fe (%)	Fe/Al[a]	S_{BET} (m^2 g^{-1})
Fe–MFI	H-ZSM-5	12.5	1.67	0.22	406
Fe–MFI-t2	H-ZSM-5	12.9	1.65	0.23	422
Fe–MFI-t4	H-ZSM-5	14.0	1.58	0.24	416
Fe–MFI-t6	H-ZSM-5	14.2	1.55	0.23	407
Fe–MFI-t8	H-ZSM-5	14.3	1.54	0.23	424

[a] Molar ratio.

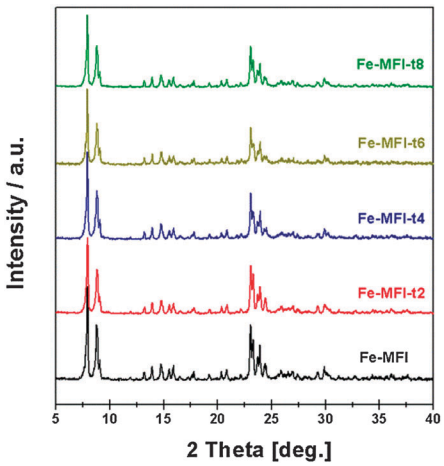

Fig. 1 XRD patterns of Fe–MFI employed in this study.

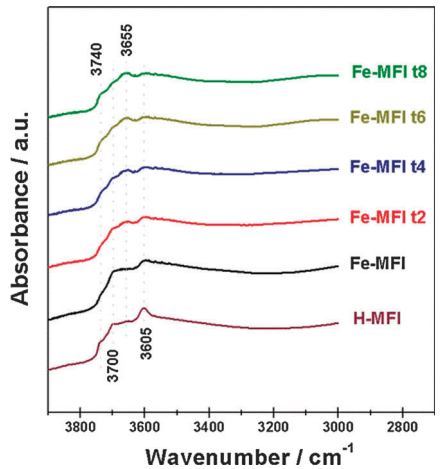

Fig. 2 DRIFT spectra of H–MFI and Fe–MFI samples.

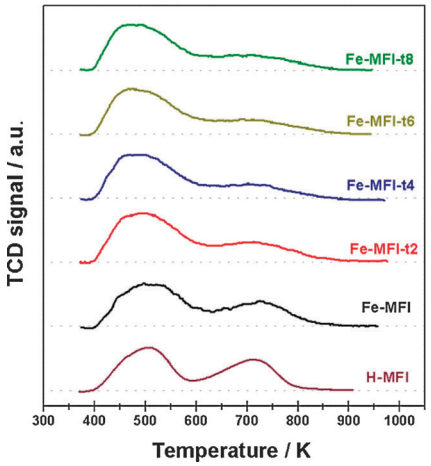

Fig. 3 NH_3-TPD profiles of Fe–MFI samples before and after acid post-treatments.

replacement of protons in Brønsted acid hydroxyl groups by cationic iron species, in consistency with the FTIR spectra in Fig. 2. It can also be noted that the amount of Brønsted acid sites in Fe–MFI gradually decreases with accumulative acid post-treatments, which should be ascribed to the continuous dealumination in the MFI framework.

The ^{27}Al MAS-NMR spectra of Fe–MFI samples before and after acid treatments are shown in Fig. 4. For Fe–MFI, a strong signal at *ca.* 55 ppm corresponding to tetrahedrally coordinated aluminum at non-equivalent framework positions and a very weak signal at *ca.* 0 ppm corresponding to octahedrally coordinated extra-framework aluminum species[27] can be observed. Accumulative acid post-treatments on Fe–MFI result in a slight increase in the intensity of the NMR signal at *ca.* 0 ppm, indicating the dealumination upon acid treatments. Based on the results from DRIFT spectra in the hydroxyl stretching region (Fig. 2), NH_3-TPD (Fig. 3), ^{27}Al MAS-NMR spectra

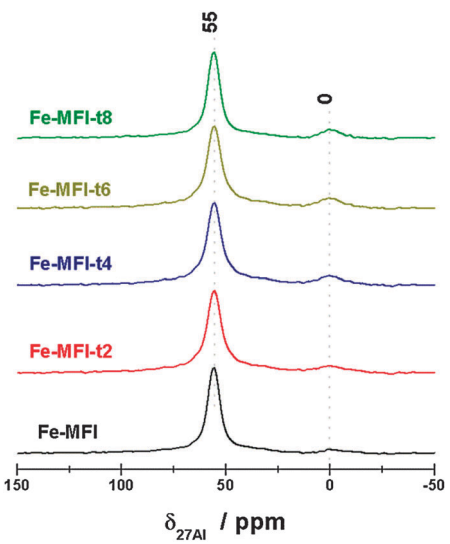

Fig. 4 ^{27}Al MAS-NMR spectra of Fe–MFI samples before and after acid post-treatments.

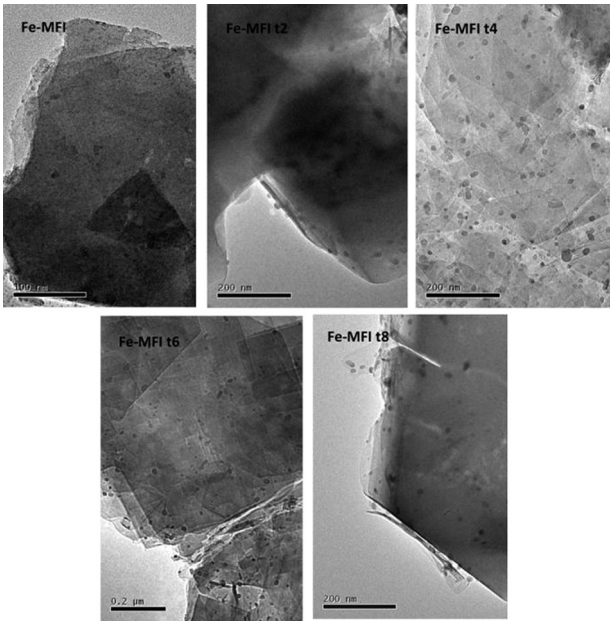

Fig. 5 TEM images of Fe–MFI samples before and after acid post-treatments.

(Fig. 4) and ICP analysis (Table 1), the framework dealumination of Fe–MFI upon acid post-treatments can be unambiguously confirmed. Some of the aluminum species removed from the framework leach to the liquid phase during acid treatments as proved by the increasing Si/Al ratios in Table 1, while others exist in the form of extra-framework species in Fe–MFI as proved by ^{27}Al MAS-NMR spectra in Fig. 4.

TEM analysis is employed to give a direct view on the formation of iron-related phase in Fe–MFI and acid treated Fe–MFI samples. In the TEM image of Fe–MFI in Fig. 5, nanoparticles with sizes of 2–6 nm are observed to disperse on the surface of MFI zeolite. These nanoparticles should consist of iron oxides that are formed during ion exchange and the subsequent calcination process. In the TEM image of Fe–MFI-t*n*, more nanoparticles with the larger sizes of 3–10 nm can be observed. The first impression is that serious aggregation of iron oxide nanoparticles occurs during acid post-treatment and calcination. A reasonable explanation is that dealumination in the MFI framework occurs during acid post-treatments on Fe–MFI and the presence of extra-framework aluminum species may induce the epitaxial growth of the iron oxides, as suggested by Prins *et al.*[28]

3.2 Characterization of iron sites in Fe–MFI

The H_2-TPR profiles of Fe–MFI samples are shown in Fig. 6 and the existence of reducible iron species is revealed in some cases. According to the literature reports,[29,30] the peaks of H_2 consumption below 750 K correspond to the reduction of ferric ions to ferrous ions in isolated state, oligonuclear clusters and nanoparticles with a H/Fe ratio of 1, and the peaks of H_2 consumption at 750–1000 K correspond to the reduction of ferrous ions to metallic iron in nanoparticles species with a H/Fe ratio of 2. The reduction of ferrous ions to metallic iron in

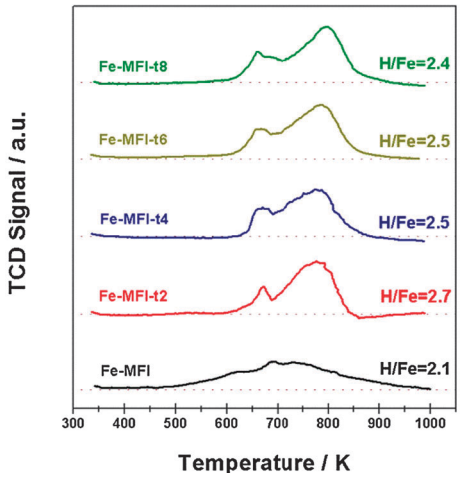

Fig. 6 H_2-TPR profiles of Fe–MFI samples before and after acid post-treatments.

isolated state and oligonuclear clusters will be accompanied by the collapse of zeolite framework and the peaks of H_2 consumption should appear well over 1000 K. For Fe–MFI, broad H_2 consumption peaks from 500 to 1000 K with total H/Fe ratio of 2.1 are observed, indicating the existence of various iron sites, *e.g.* isolated ferric ions/oligonuclear clusters and nanoparticles. Through acid treatment, the intensities of H_2 consumption peaks below 750 K decrease, while the intensities of H_2 consumption peaks at 750–1000 K increase. The total H/Fe ratio increases distinctly from 2.1 to 2.7, indicating the formation of more nanoparticles through acid treatment. Moreover, accumulative acid post-treatments do not lead to obvious changes in the TPR profiles and H/Fe ratios of 2.4–2.7 are obtained.

UV-Vis spectroscopy is a common technique for the characterization of iron sites in Fe–zeolite and the O → Fe ligand to metal charge transfer transitions can give useful information on the coordination states and aggregation extent of iron species. The UV-Vis spectra of Fe–MFI samples before and after acid treatments are shown in Fig. 7. It is seen that all Fe–MFI samples exhibit strong absorbance in 200–700 nm, revealing the existence of various ferric ions. Specifically, the UV bands at below 300 nm are assigned to isolated ferric ions in tetrahedral coordination (at 215 and 245 nm) or isolated ferric ions in octahedral coordination (at 275 nm).[31,32] The UV bands at below 300 nm can also arise from ferric ion dimers when Fe–zeolite samples are hydrated and the antiferromagnetic coupling is weak.[33] The UV bands between 300 and 400 nm are assigned to octahedral ferric ions in oligonuclear Fe_xO_y clusters, while the UV bands at above 400 nm are due to the formation of large Fe_2O_3 nanoparticles.[34] Despite the existing controversies on the assignments of UV-Vis subbands, it is quite clear that ferric ions with different nuclearity, *e.g.* isolated ions, oligonuclear clusters and Fe_2O_3 nanoparticles, are obtained after ion exchange and subsequent calcination. Through acid post-treatments, the percentage of Fe_2O_3 nanoparticles increases to some extent, in great consistent with TEM observations. However, no obvious differences can be observed on Fe–MFI after acid treatments for different times.

The EPR spectra of Fe–MFI samples before and after acid treatments are shown in Fig. 8. For calcined Fe–MFI, EPR signals at $g' = 2.0$ and $g' = 4.3$ can be observed. The $g' = 2.0$ EPR signal should be originated from highly symmetric isolated ferric ions and/or small oligomers with weak dipolar coupling, while the $g' = 4.3$ signal should be originated from the ferric ions in tetrahedral coordination.[35,36] Through acid post-treatments, the intensity of $g' = 2.0$ EPR signal decreases, while the intensity of $g' = 4.3$ EPR signal increases. Further accumulative acid post-treatments result in the appearance of $g' = 5.6$ and $g' = 6.4$ EPR signals, which should be assigned to isolated ferric ions in higher coordination, *i.e.* with five or six neighboring oxygen ions.[36] Obviously, the iron sites in Fe–MFI undergo transformation during acid post-treatments and subsequent calcination. The EPR spectra of uncalcined Fe–MFI samples (dried at 353 K) are also shown in Fig. 8. For Fe–MFI prepared by ion exchange with ferrous salt, ferrous ions should be the initial iron species introduced to MFI host. EPR signals corresponding to various ferric ions are observed on uncalcined

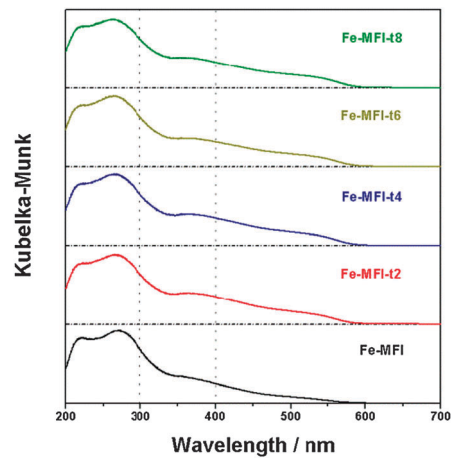

Fig. 7 UV-Vis spectra of Fe–MFI samples before and after acid post-treatments.

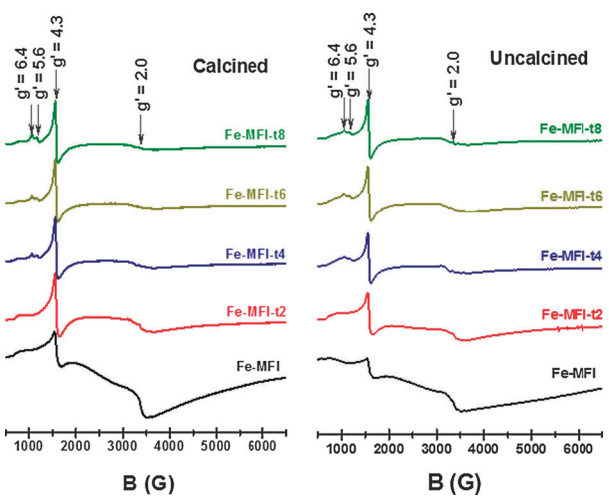

Fig. 8 EPR spectra of Fe–MFI samples before and after acid post-treatments.

Fe–MFI samples due to the oxidation of ferrous ions to ferric ions during the drying process. Moreover, the observed EPR signals on uncalcined samples are quite similar with those on calcined samples, indicating that the transformation of iron species occurs mainly during the acid post-treatment step instead of subsequent calcination step.

According to the commonly adopted model, three different extra-framework sites for isolated metal ions can be identified in zeolite MFI: α site in the straight channels, β site in the intersection between straight and sinusoidal channels and boat-shape γ site in the sinusoidal channels.[37,38] Further researches of Brückner *et al.* have correlated the different EPR signals to the different sites located in ion exchanged Fe–ZSM-5 based on the characteristic redox behavior of iron species.[36] Particularly, the $g' = 4.3$ EPR signal is attributed to the γ sites in the sinusoidal channels, the $g' = 5.6$ and $g' = 6.4$ EPR signals to the β sites in the intersection between straight and sinusoidal channels, and the $g' = 2.0$ EPR signal to the α site in the straight channels as well as small oligomers in the straight channels of ZSM-5 structure. In the present study, we would like to follow the conclusions and the EPR results indicate the migration of iron species in the channels of ZSM-5 during acid post-treatments, *i.e.* from the straight channels to the sinusoidal channels.

FTIR spectroscopy with NO probe is an informative and sensitive technique for the characterization of iron sites in zeolite.[39–42] The characteristic of this technique lies in that only exposed iron sites can be explored, while iron sites in sub-surface position or buried inside cannot be detected. Thus, it can provide us with necessary information on the available or so-called working iron sites in catalytic reactions. It should also be mentioned that the adsorption of NO on oxidized ferric ions is negligible at room temperature, and nitrosyls are formed exclusively with the participation of ferrous ions.[39] Therefore, the Fe–MFI samples employed for FTIR analysis in this study are pre-treated at elevated temperature under inert atmosphere to induce the auto-reduction of ferric ions to ferrous ions.[24,43] Fig. 9 shows the FTIR spectra of Fe–MFI samples in flowing He after exposure to 1% NO for 10 min at room temperature. NO adsorption on Fe–MFI results in a broad band centered at 1840 cm^{-1}. Through acid post-treatments, the broad band at 1840 cm^{-1} shifts slightly to higher wavenumbers, and two new IR bands at 1875 and 1880 cm^{-1} appear. According to literature reports, the band at 1875 cm^{-1} is assigned to mono-nitrosyl on extra-framework Fe^{2+}–O–Al species,[42,44] while the band at 1880 cm^{-1} is assigned to mono-nitrosyl on isolated ferrous ions located at the γ sites of ZSM-5 structure.[45,46] The IR bands at around 1850 cm^{-1} should be originated from mono-nitrosyl on ferrous ions, while the location of specific site is a matter of debate. Joyner *et al.*[47] assigned the band at 1841 cm^{-1} to mono-nitrosyl on isolated ferrous ions, and Lezcano *et al.*[48] further assigned the band at 1838 cm^{-1} to mono-nitrosyl on isolated ferrous ions located at the α sites of ZSM-5. Mul *et al.*[42] assigned the IR band at 1853 cm^{-1} to mono-nitrosyl on ferrous ions in oligonuclear clusters probably in the straight channels of ZSM-5. For Fe–ZSM-5 prepared by aqueous-phase ion exchange, the straight channels of ZSM-5 zeolite favor the diffusion of iron precursor and the formation of clusters is unavoidable during the calcination step. Therefore, we prefer to assign the band at 1840 cm^{-1} to mono-nitrosyl on ferrous ions in oligonuclear clusters in the straight channels of ZSM-5 zeolite. The shifts of 1840 cm^{-1} band to higher wavenumbers should be ascribed to the changes in the environment and nuclearity of oligonuclear clusters through acid post-treatments. Based on the FTIR spectra with NO adsorption, it is evident that iron species in Fe–MFI undergo auto-reduction, *i.e.* ferric ions to ferrous ions, upon high-temperature treatment under inert atmosphere. It should be mentioned that not all ferric ions can be auto-reduced to ferrous ions and some inert ferric ions, probably those strongly interact with zeolite framework, can remain in their ferric form after high-temperature treatment under inert atmosphere. Since the activation of nitrous oxide is facilitated on ferrous ions,[49,50] the "inert" ferric ions, *i.e.* those cannot be auto-reduced at elevated temperature, will not play a major role in N_2O-involved reaction. Acid post-treatments on Fe–MFI samples result in the dealumination in ZSM-5 framework and lead to the formation of extra-framework Fe–O–Al species. Moreover, the detectable ferrous ions migrate from the straight channels to the sinusoidal channels during acid post-treatments, in consistent with the migration of iron species revealed by EPR spectra.

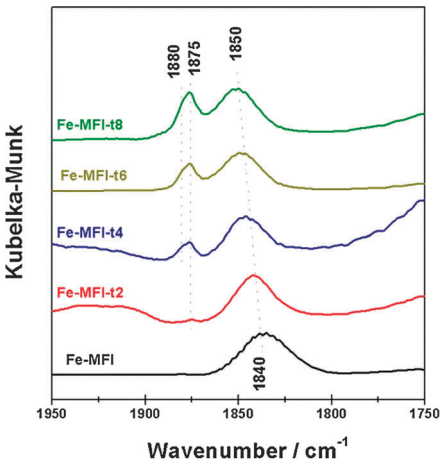

Fig. 9 FTIR spectra of NO adsorption on Fe–MFI samples before and after acid post-treatments.

3.3 Catalytic performances of Fe–zeolites

Fe–zeolites with similar Si/Al ratios and different framework structures are studied as possible catalysts for the ODHP with nitrous oxide. Fe–FER and Fe–MOR exhibit quite low activity for the ODHP with nitrous oxide, while Fe–BEA, Fe–FAU and Fe–MFI exhibit significant ODHP activity (Fig. S2, ESI†). Undoubtedly, the framework structure of Fe–zeolite plays a decisive role in the catalytic activity. Fe–MFI appears to be more promising catalyst for the ODHP with nitrous oxide and a maximal propylene yield of *ca.* 14% can be obtained at 673 K. The major by-products from ODHP with nitrous oxide are CO and CO_2, while trace acrolein and some other oxygenates can be also detected.

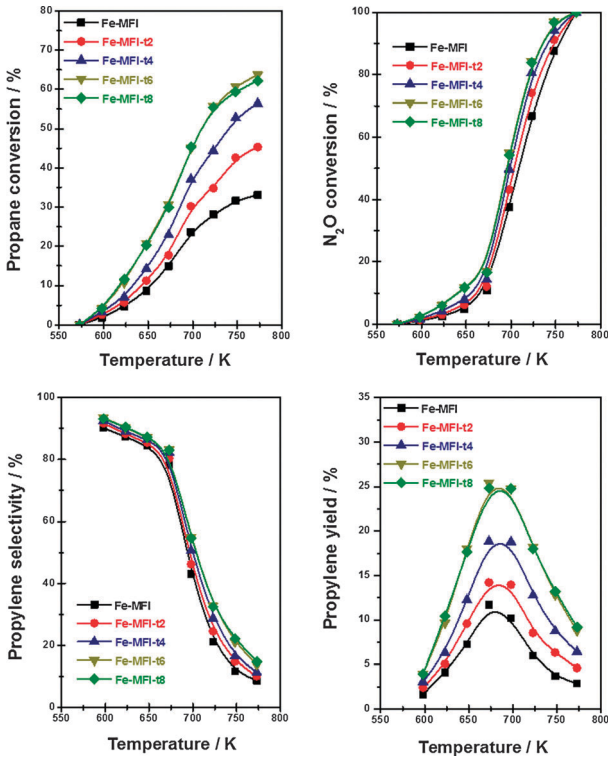

Fig. 10 ODHP with nitrous oxide catalyzed by Fe–MFI samples before and after acid post-treatments. Reaction conditions: 7.5% C_3H_8, 15% N_2O and He balance; GHSV = 15 000 h^{-1}.

Fig. 10 displays the ODHP with nitrous oxide catalyzed by Fe–MFI samples before and after acid post-treatments. For Fe–MFI, the propane conversion increases while the propylene selectivity decreases with increasing reaction temperature from 573 to 773 K, resulting in a volcano plot of propylene yield with a maximum at 673 K. Meanwhile, the nitrous oxide conversion increases from 0 to 100% with increasing reaction temperature. Acid post-treatments on Fe–MFI enhance both the propane conversion and the propylene selectivity to some extent, and therefore, promote the ODHP with nitrous oxide. The promotion effects are more obvious with accumulative acid post-treatments up to six times and further acid post-treatments do not contribute to the propylene production. Typically, the maximal propylene yield increases from *ca.* 12% over Fe–MFI to *ca.* 25% over Fe–MFI-t6 and Fe–MFI-t8. It should be mentioned that the propylene yield of *ca.* 25% obtained in the present work are comparable with the best results reported for iron–zeolite catalysts under similar conditions.[13–15,26]

Fig. 11 displays the results of nitrous oxide decomposition over Fe–MFI samples before and after acid post-treatments. For Fe–MFI, nitrous oxide decomposition starts at 698 K and then the nitrous oxide conversion increases with increasing reaction temperature. Accumulative acid post-treatments on Fe–MFI show mild positive effects on the activity for nitrous oxide decomposition and the nitrous oxide conversion at 773 K increases from *ca.* 35% of Fe–MFI to *ca.* 55% of Fe–MFI-t8. However, the nitrous oxide conversion is very low (<2%) at 673 K, the temperature when maximal propylene yield is obtained in the

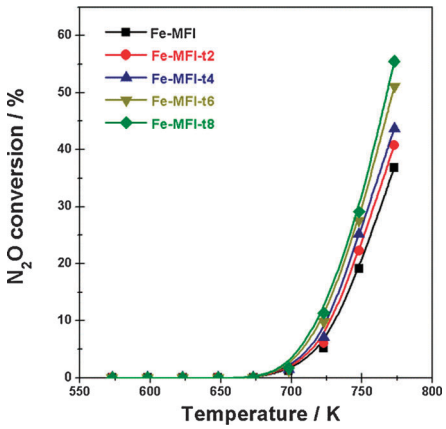

Fig. 11 Nitrous oxide decomposition catalyzed by Fe–MFI samples before and after acid post-treatments. Reaction conditions: 15% N_2O and He balance; GHSV = 15 000 h^{-1}.

oxidative dehydrogenation of propane with nitrous oxide. It is thus indicated that the presence of propane in the reaction system greatly improves the conversion of nitrous oxide catalyzed by Fe–MFI.

The deactivation and regeneration of Fe–MFI-t8 catalyst in the ODHP with nitrous oxide are further investigated. As shown in Fig. 12, Fe–MFI-t8 suffers from severe deactivation during the progress of reaction and the propylene yield decreases from *ca.* 26% to *ca.* 12% within time-on-stream of 240 min. Based on the literature reports, the deactivation of Fe–zeolites in the ODHP with nitrous oxide should be caused by the formation of coke on the surface of catalysts.[17,18] In our experiment, coke with weight content of *ca.* 9.5% is observe to accumulate on Fe–MFI-t8 after ODHP reaction for 240 min. Thereupon, coke-burning regeneration is performed on the deactivated catalyst by calcination in 15% N_2O at 773 K for 120 min. After regeneration, the activity of Fe–MFI-t8 catalyst in the ODHP with nitrous oxide can fully recover to the initial level. Moreover, the regenerated catalyst exhibits similar deactivation behavior to the fresh catalyst, indicating the good regeneration property of Fe–MFI-t8.

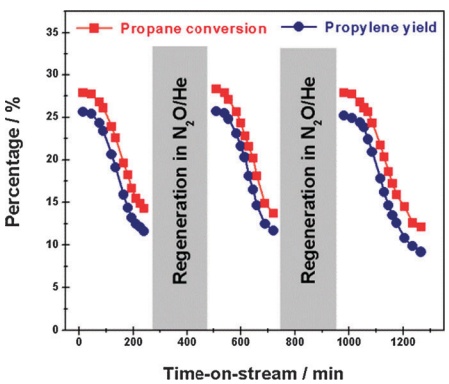

Fig. 12 Deactivation and regeneration of Fe–MFI-t8 catalyst in the ODHP with nitrous oxide at 673 K. Reaction conditions: 7.5% C_3H_8, 15% N_2O and He balance; GHSV = 15 000 h^{-1}.

4. Discussion

4.1 Transformation of iron species in Fe–MFI during acid post-treatment

Through solution ion exchange with ferrous salt, extra-framework iron species can be introduced to the zeolite host. Based on the characterization results from H_2-TPR (Fig. 6), UV-Vis (Fig. 7) and EPR (Fig. 8), ferric ions with different nuclearity, *e.g.* isolated ions, oligonuclear clusters and Fe_2O_3 nanoparticles, are obtained after ion exchange and subsequent calcination. The ion exchange results obtained here are consistent with literature reports on Fe–MFI prepared *via* similar route.[34,36] In the present study, acid post-treatments are performed on Fe–MFI to induce the framework dealumination and the corresponding changes in the iron site constitution in Fe–MFI. As expected, post-treatments in diluted acid solution show significant impacts on the properties of Fe–MFI sample. Although the framework structure of MFI zeolite is well preserved after acid post-treatment (ref. XRD patterns in Fig. 1), the dealumination in MFI framework occurs and the Si/Al ratio increases slightly (Table 1). The framework dealumination leads to significant decrease in Brønsted acid sites (ref. the DRIFT spectra in Fig. 2) and the increase in the extra-framework aluminum species (^{27}Al MAS-NMR in Fig. 4). The reduction of strong acid sites (NH_3-TPD profiles in Fig. 3) is beneficial to reduce the further reaction of propylene and therefore enhance the selectivity to propylene in ODHP (Fig. 10), in consistence with the results reported by Ates *et al.*[26] Accompanied by the dealumination process, the leaching of iron species during acid post-treatment is evident, as indicated by the decreases in iron loadings (Table 1). On the one hand, the leached iron species, together with leached aluminum species, may adsorb on the iron oxides at the outer surface of MFI and induce the epitaxial growth of the iron oxides. This results in the formation of more and larger iron oxide nanoparticles, as revealed by the TEM images in Fig. 5 and UV-Vis spectra in Fig. 7. On the other hand, the leached iron species may act as iron source and re-exchange process takes place inside the MFI channels during acid post-treatment. This results in the migration of iron species from the straight channels to the sinusoidal channels in MFI, as revealed by the EPR spectra in Fig. 8. Based on the data presented in Table 1, accumulative acid post-treatments up to six times lead to the more significant leaching of iron and aluminum species, as well as the continuous migration of iron species from the straight channels to the sinusoidal channels in MFI (Fig. 8). Meanwhile, the iron oxides nanoparticles do not show obvious changes with the progress of accumulative acid post-treatment.

4.2 Active iron sites for propane dehydrogenation with nitrous oxide

The exposed iron sites in Fe–MFI are probed by FTIR spectra of NO adsorption and nitrosyls on auto-reduced ferrous ions are employed for the titration of iron sites. As shown in Fig. 8, the ferrous ions in oligonuclear clusters change slightly, while the formation of extra-framework Fe^{2+}–O–Al species and isolated ferrous ions located at the γ sites of ZSM-5 structure are quite evident during accumulative acid post-treatments. It has been reported that oligonuclear iron species are preferred over isolated iron species for nitrous oxide decomposition due to the easier oxygen combination.[51,52] In the present study, similar nitrous oxide decomposition activities are obtained for Fe–MFI before and after acid post-treatments (Fig. 11), indicating that oligonuclear iron species plays a major role in nitrous oxide decomposition. It should be noted that the direct decomposition of nitrous oxide takes place at above 673 K (Fig. 11), while significant nitrous oxide conversion can be observed in the oxidative dehydrogenation of propane with nitrous oxide at below 673 K (Fig. 10). The equimolar reaction between nitrous oxide and propane is the desired pathway for the ODHP ($N_2O + C_3H_8 \rightarrow C_3H_6 + N_2 + H_2O$). This reaction contains two steps: (1) the chemisorption of nitrous oxide and (2) the removal of deposited oxygen by propane (* indicates the active site).

$$N_2O + * \rightarrow N_2 + *{-}O \quad (1)$$

$$*{-}O + C_3H_8 \rightarrow C_3H_6 + H_2O + * \quad (2)$$

Since nitrous oxide easily chemisorbs on iron sites in iron–zeolites, the reactivity of deposited oxygen toward propane determines the dehydrogenation activity. Based on the correlation between the exposed iron sites in Fe–MFI characterized by FTIR spectra of NO adsorption (Fig. 9) and the ODHP activity (Fig. 10), we believe that extra-framework Fe–O–Al species and/or isolated iron species in the sinusoidal channels of MFI are more active species than oligonuclear iron species for ODHP with nitrous oxide. Unfortunately, current experiment data cannot give us exact information on either extra-framework Fe–O–Al species or isolated iron species in the sinusoidal channels of MFI is more important for the reaction. However, since steam activated Fe–ZSM-5 is more active than steam activated Fe–silicalite in the ODHP with nitrous oxide,[14–17] it is reasonable to suppose that extra-framework Fe–O–Al species plays an essential role in the reaction. Therefore, it is instructive to drive iron species at framework positions or cation sites to extra-framework Fe–O–Al species in order to obtain highly active iron–zeolite catalyst for the ODHP with nitrous oxide.

5. Conclusion

Fe–MFI prepared by reductive solution ion-exchange is active catalyst for the ODHP with nitrous oxide and maximal propylene yield of *ca.* 14% can be obtained at 673 K. Acid post-treatments on Fe–MFI show distinct positive effects on the activity in the ODHP with nitrous oxide. Typically, the maximal propylene yield gradually increases to *ca.* 25% with accumulative acid post-treatments.

Characterization results reveal that ferric ions with different nuclearity, *e.g.* isolated ions, oligonuclear clusters and Fe_2O_3 nanoparticles, are formed in Fe–MFI after reductive solution ion-exchange and subsequent calcination. Acid post-treatments on Fe–MFI show significant impacts on the properties of Fe–MFI sample. The leaching of iron and aluminum species is clearly observed during acid post-treatments. Meanwhile, the leached iron species can act as iron source and re-exchange

process takes place inside the MFI channels during acid post-treatment, resulting in the migration of iron species from the straight channels to the sinusoidal channels in MFI.

The exposed iron sites in Fe–MFI are probed by FTIR spectra of NO adsorption. The oligonuclear iron species the straight channels is detected in Fe–MFI, while acid post-treatments result in the appearance of extra-framework Fe–O–Al species and isolated iron species in the sinusoidal channels. Based on the correlation between the exposed iron sites and the dehydrogenation activity, we propose that extra-framework Fe–O–Al species and/or isolated iron species are more active species than oligonuclear iron species for propane dehydrogenation with nitrous oxide.

Acknowledgements

This work is financially supported by the National Basic Research Program of China (2009CB623502) and 111 Project (B12015). The support from the Ministry of Education of China (NCET-11-0251) is also acknowledged.

Notes and references

1 F. C. Meunier, A. Yasmeen and J. R. H. Ross, *Catal. Today*, 1997, **37**, 33.
2 J. G. Eon, R. Olier and J. C. Volta, *J. Catal.*, 1994, **145**, 318.
3 G. I. Panov, A. K. Uriarte, M. A. Rodkin and V. I. Sobolev, *Catal. Today*, 1998, **41**, 365.
4 L. V. Pirutko, V. S. Chernyavsky, A. K. Uriarte and G. I. Panov, *Appl. Catal., A*, 2002, **227**, 143.
5 P. Kubánek, B. Wichterlová and Z. Sobalík, *J. Catal.*, 2002, **211**, 109.
6 E. J. M. Hensen, Q. Zhu and R. A. van Santen, *J. Catal.*, 2003, **220**, 260.
7 J. Jia, K. S. Pillai and W. M. H. Sachtler, *J. Catal.*, 2004, **221**, 119.
8 K. Yoshizawa, Y. Shiota, T. Yumura and T. Yamabe, *J. Phys. Chem. B*, 2000, **104**, 734.
9 B. R. Wood, J. A. Reimer, A. T. Bell, M. T. Janicke and K. C. Ott, *J. Catal.*, 2004, **225**, 300.
10 E. V. Starokon, M. V. Parfenov, L. V. Pirutko, S. I. Abornev and G. I. Panov, *J. Phys. Chem. C*, 2011, **115**, 2155.
11 K. Nowińska, A. Wacław and A. Izbińska, *Appl. Catal., A*, 2003, **243**, 225.
12 R. Bulánek, B. Wichterlová, K. Novoveská and V. Kreibich, *Appl. Catal., A*, 2004, **264**, 13.
13 J. Pérez-Ramírez and A. Gallardo-Llamas, *J. Catal.*, 2004, **223**, 382.
14 E. V. Kondratenko and J. Pérez-Ramírez, *Appl. Catal., A*, 2004, **267**, 181.
15 J. Pérez-Ramírez and A. Gallardo-Llamas, *Appl. Catal., A*, 2005, **279**, 117.
16 J. Pérez-Ramírez and A. Gallardo-Llamas, *J. Phys. Chem. B*, 2005, **109**, 20529.
17 O. Sánchez-Galofré, Y. Segura and J. Pérez-Ramírez, *J. Catal.*, 2007, **249**, 123.
18 W. Wei, J. A. Moulijn and G. Mul, *J. Catal.*, 2009, **262**, 1.
19 J. Kowalska-Kus, A. Held and K. Nowinska, *Catal. Lett.*, 2010, **136**, 199.
20 M. M. J. Treacy and J. B. Higgins, *Collection of simulated XRD powder patterns for zeolites*, Elsevier, Fifth Revised Edn, 2007.
21 O. Cairona, K. Thomasb and T. Chevreau, *Microporous Mesoporous Mater.*, 2001, **46**, 327.
22 L. Li and N. Guan, *Microporous Mesoporous Mater.*, 2009, **117**, 450.
23 Q. Zhu, B. L. Mojet, R. A. J. Janssen, E. J. M. Hensen, J. van Grondelle, P. C. M. M. Magusin and R. A. van Santen, *Catal. Lett.*, 2002, **81**, 205.
24 L. J. Lobree, I.-C. Hwang, J. A. Reimer and A. T. Bell, *J. Catal.*, 1999, **186**, 242.
25 M. Iwasaki, K. Yamazaki, K. Banno and H. Shinjoh, *J. Catal.*, 2008, **260**, 205.
26 A. Ates, C. Hardacre and A. Goguet, *Appl. Catal., A*, 2012, **441–442**, 30.
27 P. Marturano, L. Drozdová, A. Kogelbauer and R. Prins, *J. Catal.*, 2000, **192**, 236.
28 P. Marturano, L. Drozdova, A. Kogelbauer and R. Prins, *J. Catal.*, 2000, **190**, 460.
29 A. Guzmán-Vargas, G. Delahay and B. Coq, *Appl. Catal., B*, 2003, **42**, 369.
30 L. Li, Q. shen, J. Li, Z. Hao, Z. Xu and G. Q. Lu, *Appl. Catal., A*, 2008, **344**, 131.
31 M. S. Kumar, M. Schwidder, W. Grünert and A. Brückner, *J. Catal.*, 2004, **227**, 384.
32 E. J. M. Hensen, Q. Zhu, R. A. J. Janssen, P. C. M. M. Magusin, P. J. Kooyman and R. A. van Santen, *J. Catal.*, 2005, **233**, 123.
33 G. D. Pirngruber, P. K. Roy and R. Prins, *Phys. Chem. Chem. Phys.*, 2006, **8**, 3939.
34 M. Schwidder, M. S. Kumar, K. Klementiev, M. M. Pohl, A. Brückner and W. Grünert, *J. Catal.*, 2005, **231**, 314.
35 M. Høj, M. J. Beier, J.-D. Grunwaldt and S. Dahl, *Appl. Catal., B*, 2009, **93**, 166.
36 E. Berrier, O. Ovsitser, E. V. Kondratenko, M. Schwidder, W. Grünert and A. Brückner, *J. Catal.*, 2007, **249**, 67.
37 J. Dêdeček, D. Kaucky and B. Wichterlová, *Microporous Mesoporous Mater.*, 2000, **35–36**, 483–494.
38 L. Čapek, V. Kreibich, J. Dêdeček, T. Grygar, B. Wichterlová, Z. Sobalík, J. A. Martens, R. Brosius and V. Tokarová, *Microporous Mesoporous Mater.*, 2005, **80**, 279.
39 K. Hadjiivanov, *Catal. Rev. Sci. Eng.*, 2000, **42**, 71.
40 A. Zecchina, M. Rivallan, Gl. Berlier, C. Lamberti and G. Ricchiardi, *Phys. Chem. Chem. Phys.*, 2007, **9**, 3483.
41 M. Mihaylov, E. Ivanova, N. Drenchev and K. Hadjiivanov, *J. Phys. Chem. C*, 2010, **114**, 1004.
42 G. Berlier, C. Lamberti, M. Rivallanw and G. Mul, *Phys. Chem. Chem. Phys.*, 2010, **12**, 358.
43 G. D. Pirngruber, P. K. Roy and N. Weiher, *J. Phys. Chem. B*, 2004, **108**, 13746.
44 G. Mul, J. Pérez-Ramírez, F. Kapteijn and J. A. Moulijn, *Catal. Lett.*, 2002, **80**, 129.
45 K. Sun, H. Xia, Z. Feng, R. van Santen, E. Hensen and C. Li, *J. Catal.*, 2008, **254**, 383.

46 H. Y. Chen, El-M. El-Malki, X. Wang, R. A. van Santen and W. M. H. Sachtler, *J. Mol. Catal. A: Chem.*, 2000, **162**, 159.
47 R. W. Joyner and M. Stockenhuber, *J. Phys. Chem. B*, 1999, **103**, 5963.
48 M. Lezcano, V. I. Kovalchuk and J. L. d'Itri, *Kinet. Catal.*, 2001, **42**, 104.
49 G. D. Pirngruber, *J. Catal.*, 2003, **219**, 456.
50 K. Sun, H. Xia, E. Hensen, R. van Santen and C. Li, *J. Catal.*, 2006, **238**, 186.
51 J. Pérez-Ramírez, F. Kapteijn and A. Brückner, *J. Catal.*, 2003, **218**, 234.
52 J. Pérez-Ramírez, *J. Catal.*, 2004, **227**, 512.

